

Picocavity-enhanced near-field optical microscopy with 1 nm resolution

Akitoshi Shiotari^{1*}, Jun Nishida^{2,3}, Adnan Hammud⁴, Fabian Schulz⁵,
Martin Wolf¹, Takashi Kumagai^{2,3}, Melanie Müller¹

¹Department of Physical Chemistry, Fritz-Haber Institute of the Max-Planck Society,
Faradayweg 4–6, 14195 Berlin, Germany.

²Institute for Molecular Science, National Institutes of Natural Sciences,
38 Nishigonaka, Myodaichi-cho, 444-8585 Okazaki, Japan.

³The Graduate University for Advanced Studies, SOKENDAI, Shonan Village, 240-0193 Hayama, Japan.

⁴Department of Inorganic Chemistry, Fritz-Haber Institute of the Max-Planck Society,
Faradayweg 4–6, 14195 Berlin, Germany.

⁵CIC NanoGUNE, Tolosa Hiribidea 76, 20018 Donostia–San Sebastián, Spain.

*Corresponding author. Email: shiotari@fhi-berlin.mpg.de

Scattering-type scanning near-field optical microscopy (s-SNOM) allows for the observation of the optical response of material surfaces with a resolution far below the diffraction limit. A spatial resolution of 10–100 nm is routinely achieved in s-SNOM based on amplitude-modulation atomic force microscopy (AM-AFM) with tapping amplitudes of tens of nanometers. However, optical imaging and spectroscopy of structures that are localized to the atomic scale remain a significant challenge. This can be overcome by combining the field enhancement localized at the atomic-scale structure of the tip apex, namely a plasmonic picocavity, with frequency-modulation AFM (FM-AFM), namely non-contact AFM, in

a stable cryogenic ultrahigh vacuum environment. Here, we developed picocavity-enhanced SNOM (PE-SNOM) under visible laser illumination based on the integration of a quartz tuning fork sensor with small-amplitude oscillations of 1 nm or less. In addition, the use of a focused ion beam-polished silver tip mounted on the sensor leads to strong field enhancement in the picocavity and ensures minimal background scattering from the tip shaft. PE-SNOM allows us to obtain a material-contrast image of silicon islands on a silver surface with 1-nm lateral resolution, which surpasses the conventional limits of s-SNOM. PE-SNOM paves the way for the acquisition of optical information from atomic-scale targets, such as single photo-active defects and molecules.

Introduction

The combination of optical spectroscopy with scanning tunneling microscopy (STM) enables the optical characterization of material surfaces, nanostructures and molecules as well as their optical control with a resolution far beyond the diffraction limit of light (1–3). Using plasmonic STM tips, near-field optical techniques in low-temperature (LT) STM (4, 5) have been successfully applied to realize optical spectroscopy at the single- or even sub-molecular level, including tip-enhanced Raman spectroscopy (6, 7), STM-induced luminescence (8, 9), and tip-enhanced photoluminescence spectroscopy (10, 11). Moreover, the plasmonic near-fields in STM junctions allow for controlling single-molecule photoreactions (12–15) and visualizing photocurrents through molecular orbitals (16). A crucial aspect of these experiments is the extreme spatial confinement of the plasmonic field by the atomistic structure of the STM tip, giving rise to the formation of so-called plasmonic picocavities (17–19), which rest on the tens-of-nanometer-sized tip apex forming a larger nanocavity around the picocavity. This extreme confinement leads to both a localization of the incident light to the atomic scale and a very strong enhancement of optical light emission and scattering from the junction (5). While atomic-scale structures of the tip apex are thermally unstable at room temperature (20, 21), operation at LT and under ultrahigh vacuum (UHV) conditions facilitates the stable formation of such picocavities.

In parallel to the aforementioned picocavity/nanocavity-based STM studies, scanning near-field

optical microscopy (SNOM) has been established as a standard tool for measuring the local dielectric response of materials. The most well-established and sensitive approach is scattering-type SNOM (s-SNOM) (22, 23), where amplitude-modulation atomic force microscopy (AM-AFM), also known as tapping-mode AFM, is used to modulate the localized near-field light at the tapping frequency and then detect the demodulated scattering signal at higher harmonics of the tapping frequency using a lock-in amplifier (24, 25). This scheme eliminates contributions from the far-field background and outputs the part of the scattering signal that strongly depends on the tip-sample gap distance. This method has enabled the visualization of surface plasmon and phonon polaritons (26–29), phase transitions (30, 31), and individual biological molecules/complexes (32, 33), as well as in probing ultrafast dynamics at the nanoscale (34–36).

The spatial resolution of conventional s-SNOM is typically limited to tens of nanometers and in the best cases 5- or 6-nm resolution was reported (33, 37, 38). While this resolution is sufficient for many applications including the observation of polariton wavelengths longer than ~ 50 nm (28), s-SNOM has not yet accessed to more localized structures such as single molecules (39) and photo-active point defects (40). Increasing the spatial resolution to the Ångström scale remains an outstanding challenge and major goal in s-SNOM and other scattering-light detection techniques (37, 38, 41–45).

To detect light scattering from near-fields localized to the Ångström scale, a sufficiently small amplitude of the cantilever oscillation is required (see a schematic illustration in Fig. 1A). Otherwise, the duty cycle for near-field interaction is very low due to the large movement of the tip away from the surface during an oscillation cycle, significantly reducing the sensitivity to highly localized signals from ultra-narrow tip-sample gaps (46). However, AM-AFM inherently requires tapping amplitudes greater than ~ 10 nm to prevent the tapping tip from adhering to the sample surface. This problem can be overcome by frequency-modulation AFM (FM-AFM) (47), also known as non-contact AFM, using a quartz tuning fork (QTF) sensor as a cantilever (48). The stiffness of the cantilever and the constant oscillation-amplitude feedback in the FM mode allow for a stable oscillation with a small amplitude ($A \lesssim 1$ nm) (49). Operation in LT-UHV environments not only leads to high force sensitivity for FM-AFM with high Q values of the oscillation, but also allows for the formation of a stable picocavity as used in LT-STM. Recently, the advantage of combining optical excitation with hybrid STM/FM-AFM systems has been demonstrated in the low-frequency

THz regime (50).

In this study, we demonstrate FM-AFM-based s-SNOM with a controlled plasmonic picocavity, which we refer to as picocavity-enhanced SNOM (PE-SNOM). This enables the generation and detection of extremely localized scattered light with unprecedented sensitivity. Whereas previous works have demonstrated individual aspects such as SNOM with plasmon-resonant tips (51–53), at LT (31, 54, 55), with QTF sensors (56, 57), or in the FM mode (58), we integrate all those indispensable advances in PE-SNOM to achieve high-resolution optical imaging. The combination of s-SNOM and picometer-scale plasmonics paves the way for the future advancement of single-molecule and atomic-scale optical microscopy.

Results

PE-SNOM configuration

We performed PE-SNOM by combining the laser illumination and light detection setup with a commercial LT-UHV STM/FM-AFM setup (Fig. 1; see also Materials and Methods). A continuous-wave 633-nm laser beam enters the UHV chamber (incident power $P_{\text{inc}} = 3\text{--}6$ mW, p -polarized) and is focused on the tip–sample junction through a lens mounted inside the STM/AFM unit at 8 K (fig. S1 in the Supplementary Materials). The light scattered from the junction is collected by a second lens also installed inside the STM/AFM unit and is directed into a photodetector (PD) outside the UHV chamber to measure the power P of the scattered light. The apex of an electrochemically etched Ag tip is sharpened and polished by focused ion beam (FIB) milling (Fig. 1B) to obtain reproducible properties of the plasmonic nanocavity (15, 59) and to reduce far-field scattered light from a rough tip shaft. The tip is mounted on a QTF sensor (Fig. 1C) which allows for the simultaneous detection of the STM tunneling current I_t and the FM-AFM frequency shift Δf . When the cantilever is oscillated, the measured tunneling current is the time average over the oscillation cycle, denoted as $\langle I_t \rangle$. The current signal is used for feedback control of the tip height z (Fig. 1D) as general in QTF-based STM/FM-AFM (49). The cantilever is resonantly oscillated with a frequency $f = f_0 + \Delta f$, which is fed back by an automatic gain controller (AGC) to keep the oscillation amplitude A constant and by a phase-locked loop (PLL) to obtain Δf induced by

tip–sample interactions (47). We use a sine-wave output $\sin(2\pi ft)$ from the oscillation controller as the reference signal for the lock-in detection in real time (Fig. 1D), obtaining n -th harmonic signals S_n from the PD output.

Simultaneously recorded STM, FM-AFM, and s-SNOM signals

The localization of the near-field light inside the junction can be characterized by measuring tip-approach curves, which represents the tip-height dependence of the scattered signal at a given oscillation amplitude A . Figure 2A shows the measurement procedure. First, the Ag tip is placed over an atomically flat Ag(111) surface without cantilever oscillation and with the STM feedback closed (defined as $z = 0$; (i) in Fig. 2A). Next we open the feedback loop and retract the tip from $z = 0$ to $z = A$ (ii). We then start the sinusoidal cantilever oscillation with an amplitude of A such that the tip oscillated around the center position $z = A$ (iii). Therefore, the lowest tip height during the oscillation is equal to the set-point distance, i.e., $\min[z(t)] = 0$, ensuring that the tip does not crash into the surface when varying A . The instantaneous tip height during oscillation is expressed as $z(t) = \langle z \rangle + A \sin(2\pi ft)$, where $\langle z \rangle$ is the time-averaged tip height equal to the center of oscillation. We then sweep the tip height to acquire approach curves in the range between $\langle z \rangle = A$ and a given maximum height z' ((iv) in Fig. 2A). The approach curve of the s-SNOM signal $S_n(\langle z \rangle)$ is obtained along with the STM and FM-AFM signals.

Figures 2B to 2D show the STM signal ($\langle I_t \rangle$), FM-AFM signals (A and Δf), and the scattered laser power P together with the third-harmonics s-SNOM signal S_3 , respectively, simultaneously recorded over a Ag terrace with a set-point oscillation amplitude of 1.13 nm and during 633-nm laser illumination. Because a typical metal-tip–metal-sample gap distance during STM feedback is approximately 0.5 nm (60), we estimate the gap at $z = 1$ nm to be ~ 1.5 nm. We obtained the curves at $\langle z \rangle = 1$ to 150 nm. Only plots at $\langle z \rangle \leq 10$ nm are displayed in Fig. 2 because at larger tip heights, non-zero signals were not observed in $\langle I_t \rangle$, Δf , or S_3 (fig. S2). The time-averaged current $\langle I_t \rangle$ was detectable only at very close tip heights and shows a steep rise at $\langle z \rangle < 1.5$ nm as expected from the exponential z dependence of tunneling current (Fig. 2B). The FM-AFM system always keeps A constant (Fig. 2C, right axis) whereas Δf decreases monotonically as $\langle z \rangle$ decreases (left axis) due to attractive forces between the Ag tip and Ag sample. These tip-height dependences are

consistent with standard STM/FM-AFM operation (61), indicating that the laser illumination does not interfere the STM/FM-AFM performance.

As shown in the PD signal P (Fig. 2D, right axis), the near-field contribution to the total scattered power is faint and obscured by the noise of the PD channel, implying that P is dominated by background scattering with a constant intensity. However, lock-in detection at the third harmonic S_3 of the oscillation frequency (Fig. 2D, left axis) allows for the extraction of the near-field enhancement occurring only at very small gap distances. The steep increase of S_3 at $\langle z \rangle < 3$ nm is consistent with the spatial confinement of picocavity-derived electromagnetic fields (18, 19). Notably, the STM, FM-AFM, and s-SNOM channels exhibit different tip-height thresholds for non-zero signals ($\langle z \rangle \approx 1.5$ nm for $\langle I_t \rangle$, ~ 7 nm for Δf , and ~ 3 nm for S_3) as well as different steepness of the slopes, showing that their signals are independent and of different origins.

Optimal oscillation amplitude for PE-SNOM

As mentioned above, a small value of A is advantageous for detecting highly localized signals. In contrast, if A is too small, this will reduce the signal-to-noise ratio in the lock-in detection. It is therefore important to examine the optimal oscillation amplitude to obtain the best localization at a reasonably high signal level. For this purpose, we measure approach curves with various values of A . Figures 3A, C, and E show the approach curves of $\langle I_t \rangle$, Δf , and S_3 , respectively, recorded simultaneously over the Ag(111) surface for A between 0.1 and 5.0 nm. As a reference, $I_t(z)$ curve without cantilever oscillation is also shown (Fig. 3A, bold black curve). At the largest amplitude $A = 5.0$ nm, all signals show non-zero values at much larger tip heights (for example, $\langle z \rangle = 5$ nm for $\langle I_t \rangle$) compared to the plots at lower A values (see also Fig. 2 at $A = 1.13$ nm). This behavior can be explained by tip trajectory during oscillation, as illustrated by the sine waves depicted on top of Fig. 3A. At the closest $\langle z \rangle$, which depends on A as described above (Fig. 2A), the tip temporarily approaches the STM set-point distance during each oscillation cycle, giving rise to a non-zero signals in $\langle I_t \rangle$, Δf , and S_3 . The approach curves of $\langle I_t \rangle$ and Δf can be converted into the instantaneous tunneling current I_t (Fig. 3B) and vertical force F (Fig. 3D) at the bottom of the oscillation, i.e., $z = \min[z(t)]$, using the Sader–Sugimoto (62) and Sader–Jarvis (63) formulae, respectively. The converted curves are consistent at any A , corroborating the stable, harmonic

motion of the cantilever oscillation, which is critical to extract reliable s-SNOM signals upon demodulation. Notably, the conversions allow for the evaluation of the tunneling conductivity and interatomic force in narrow tip-sample gaps, e.g., at $z = 0$, using any A .

In contrast to the STM and FM-AFM results, s-SNOM at large A constrains the information at narrow tip-sample gaps, as indicated by the normalization of the lock-in signals described below. The scattered light intensity P which is modulated by the cantilever oscillation can be expressed by a Taylor series as

$$\begin{aligned} P[z(t)] &= P[\langle z \rangle + A \sin(2\pi ft)] \\ &= \sum_{m=0}^{\infty} \frac{1}{m!} A^m P^{(m)}(\langle z \rangle) \sin^m(2\pi ft), \end{aligned} \quad (1)$$

where $P^{(m)}(\langle z \rangle) \equiv \left. \frac{d^m P}{dz^m} \right|_{z=\langle z \rangle}$. The lock-in signal corresponds to the time-averaged value of the input signal P multiplied with a sine-wave reference signal with a frequency of nf for the n -th harmonics, i.e.,

$$S_n(\langle z \rangle) = \langle P[z(t)] \sin(2\pi nft + \phi_n) \rangle, \quad (2)$$

where ϕ_n denotes the phase difference between the input and reference signals (see Supplementary Text). From Eqs. 1 and 2, S_n is solved as

$$S_n(\langle z \rangle) = \frac{1}{n!2^n} A^n P^{(n)}(\langle z \rangle) + \sum_{i=1}^{\infty} c_{n+2i} A^{n+2i} P^{(n+2i)}(\langle z \rangle), \quad (3)$$

where c_{n+2i} denotes the coefficient for the $(n+2i)$ -th derivative component, which is much smaller than $\frac{1}{n!2^n}$ (see Supplementary Text). From Eq. 3, assuming higher order derivative components are negligibly small, the S_3 approach curve (Fig. 3E) can be normalized as $P^{(3)}(\langle z \rangle) = 48S_3/A^3$ (Fig. 3F; see also fig. S3 for other n -th harmonics curves and their normalization).

After normalization, all approach curves recorded at different A yield the same exponential $\langle z \rangle$ dependence of the near-field signal (Fig. 3F), however with different noise levels and minimum distances $\langle z \rangle$. The largest amplitude ($A = 5.0$ nm) provides high signal-to-noise ratio, but it misses the information below $\langle z \rangle \approx 5$ nm and does not allow to extract the picocavity-enhanced near-field signal. Furthermore, at such a large A , the contribution of the higher order derivative components (see the second term on the right side of Eq. 3) to S_n is no longer negligible, modifying the curve appearance from the original $P^{(n)}(\langle z \rangle)$ curve shape (see Supplementary Text). For these reasons,

too large values of A are not suitable for PE-SNOM. In contrast, at the smallest amplitude $A = 0.1$ nm, no s-SNOM signal S_3 was measurable above the noise floor (inset in Fig. 3F). Its normalized curve has an approximately 50 times higher noise intensity than the signals detected at higher A . Therefore, we conclude that amplitudes of 0.5–1 nm are optimal for the PE-SNOM experimental setup used. Note that this value depends on the intensity of light scattering from the near-field and the signal sensitivity of the light detection setup. Higher collection efficiency of the scattered light is expected to allow for s-SNOM signal detection with smaller A .

s-SNOM imaging of Si monolayer islands on Ag(111)

Finally, to demonstrate the lateral resolution and optical contrast of PE-SNOM, we use an Ag(111) surface partially covered by ultrathin Si islands (Fig. 1A). According to the STM appearance of the islands which partially cover the terrace and step edge are ascribed to amorphous Si films (64). Note that the islands appear darker in the image than the Ag terrace despite being located on the terrace. This contrast originates from the lower local density of states of Si compare to Ag, which competes with the topographic height difference. The coexistence of the Si monolayer islands and bare Ag surfaces minimizes the topographic height difference between Si and Ag (Fig. 4B), while retaining the plasmon enhancement effect between the Ag tip and Ag substrate (65).

we record simultaneous STM, FM-AFM and s-SNOM images of the sample (Figs. 4C to 4H and fig. S4). Both the QTF-based FM-AFM and the high harmonic lock-in detection require rather long acquisition times (~ 30 times slower than the scan speed in standard STM imaging mode), rendering imaging over larger areas at constant tip height challenging. Therefore, the tip height was controlled by the STM feedback loop to avoid thermal drift during the slow scan. As schematically shown in Fig. 4B, the scanned area has two Ag terraces separated by a single Ag-atomic step, both of which are partially covered by Si islands. The bare Ag terraces (regions I and III), Si islands (II and IV), and the monoatomic Ag step (between II and III) are easily identified by the contrast in the STM image (Fig. 4C). The appearances of the four regions are useful to understand the contrast in each image. Regions I and II have the same Ag terrace height, whereas regions I and III have the same Ag surface but with a different height by one Ag atomic layer, and regions I and IV have the same atom-layer numbers with different atomic species (Ag and Si) in the topmost layer.

While the STM feedback ensures a constant tip–sample gap distance on the same material (e.g., regions I and III), the Ag-tip–Ag-surface gaps are slightly narrower by ~ 50 pm than the Ag–Si gaps (orange dotted curves in Fig. 4B). The FM-AFM Δf map (Fig. 4D) shows several dark spots inside the Si islands, presumably due to Si atoms/clusters in the Si monolayer attractively interacting with the Ag tip (66). This suggests that simultaneous STM/FM-AFM/s-SNOM mapping provides complementary information on the scanned area due to the different signal origin of each image.

Figures 4E to 4H show s-SNOM images for different harmonics S_n . Interestingly, the image contrast changes with n . The images of S_1 and S_2 (Figs. 4E and 4F) are not sensitive to the presence of the Si islands but show a contrast with regions I and II (III and IV) apparently darker (brighter), similar to the contrast-inverted surface topography. At higher harmonics S_3 and S_4 (Figs. 4G and 4H), the image contrast changes as the Si islands in regions II and IV now exhibit darker than the Ag terraces in regions I and III. This strongly indicates that the images of S_3 and S_4 are sensitive to changes in the local dielectric environment caused by the Si islands.

The n dependence of the s-SNOM appearance agrees with the common understanding that the localized near-field signal is predominantly detected at high n (24, 33, 38, 43). The lower harmonics are not sensitive to the picocavity-enhanced near-field, and the topography-synchronized contrast in S_1 and S_2 is probably caused by the adjustment of the tip–sample distances at the two terraces across the Ag step (Fig. 4B) and scattering contributions from less localized fields. Hence, whereas the image appearances of S_1 and S_2 can be understood as topographic artifacts, the images of S_3 and S_4 show true optical, i.e. dielectric, material contrast. This is further corroborated by considering the effect of an atomic-scale structural change in the tip on the images. We observed an accidental tip change during the scan (black arrows in Figs. 4C to 4H), as evidenced by a sudden jump of the simultaneously recorded STM and FM-AFM signals. Because the same islands and the Ag step were observed similarly even after the change, this is attributed to a change in the atomic structure of the tip apex. Notably, this minor tip change has a significant impact on the contrast in S_3 and S_4 , but only a minor effect on S_1 . This proves that the atomic structure of the tip apex that forms the picocavity is crucial for detecting optical contrast in PE-SNOM.

Figure 4I shows S_4 approach curves recorded over the Ag and Si, also indicating that the S_4 signal over Si is smaller than that over Ag at small $\langle z \rangle$. This trend is consistent with previous calculations (25, 43) reporting that at 633 nm, Ag gives a larger scattering intensity in S_n than Si

due to the difference in the real part of the dielectric constant ($-18 + i0.5$ for Ag versus $15 + i0.2$ for Si). Considering that the image contrast originates only from a single atomic layer of Si, the contrast between the two surface regions is quite striking.

We note that our implementation of PE-SNOM is based on a self-homodyne scheme (see fig. S1), which arises from the interference between tip-localized scattering and background scattering (23). Nevertheless, the aforementioned results of the n -dependent s-SNOM images (Figs. 4E to 4H) and the consistency of the Ag/Si contrast with the numerical prediction support that the background effect alone cannot account for the observed contrast. This in part is facilitated by the FIB-polished tip and the atomically flat single-crystalline surface under UHV conditions, which significantly reduce uncontrolled scattering. PE-SNOM is, in principle, compatible with interferometric detection methods such as pseudo-heterodyne, which have been established to provide amplitude- and phase-resolved responses in a fully background-free manner (23, 67). Combining PE-SNOM with such interferometric techniques offers the potential for a full characterization of the dielectric function at the atomic scale.

Finally, we estimate the lateral resolution of s-SNOM and compare it to that of STM by taking line profiles along the images across a material boundary (37, 43, 45). Figure 4J shows the line profiles of the STM topography (upper) and the S_4 signal (lower) recorded simultaneously across an Ag–Si boundary on an identical terrace. To get long-distance profiles for reasonable curve fitting, we used another scan area with wider Ag and Si regions (fig. S4) than those in Fig. 4C. By the fitting of an error function, the boundary width is estimated to be 0.39 ± 0.26 nm for STM and 1.06 ± 0.13 nm for s-SNOM. The observed difference in the spatial resolution between STM and s-SNOM provides further evidence that the contrast in the higher-harmonics s-SNOM images is not caused by topographic tip-height changes or tip motion (68), but indeed reveals true optical contrast. The ability to resolve optical contrast with a spatial resolution as small as 1 nm in elastic light scattering provides an approach for optical surface analysis at the nearly atomic scale. For example, based on the contrast of the S_4 image, the bright spot with a diameter of ~ 2 nm (marked by the dotted circles in Figs. 4C and 4H) is not composed of Si, although it is located on an Si island, but can rather be assigned to an Ag cluster.

Discussion

We demonstrated the successful implementation and development of PE-SNOM employing light scattering from a stable plasmonic picocavity at a cryogenic temperature. We conducted FIB-polishing of a plasmonic Ag tip mounted to the QTF sensor of FM-AFM and show that the highly confined picocavity-enhanced near-field can be detected by demodulation and lock-in detection of the scattering signal at higher harmonics of the oscillation frequency of the QTF. We observe the highly localized near-field from the picocavity in a narrow tip–sample gap distance range of a few nanometers, and image the optical contrast between a bare Ag(111) surface and monoatomic Si islands on the surface with a lateral resolution of 1 nm. PE-SNOM will be of interest for the optical characterization of a wide range of conducting and insulating nanomaterials exhibiting optical and dielectric heterogeneity at the atomic scale. The integration of s-SNOM in the LT-UHV STM/FM-AFM setup enables the simultaneous detection of multiple independent observables including electric conductivity (STM), interatomic attractive/repulsive forces (FM-AFM), and dielectric constant (s-SNOM), which promises new insights into, e.g., the photophysics of single defects and molecules and the optical properties of atomically sharp interfaces.

Materials and Methods

PE-SNOM setup

PE-SNOM was performed with an LT-UHV STM/FM-AFM machine (CreaTec Fischer & Co. GmbH; base pressure $< 5 \times 10^{-11}$, sample temperature = 8 K). The optical configuration on a self-homodyne scheme is depicted in fig. S1A. The output voltage of the Si-biased PD was converted into the light power P by the calibration with a Si-photodiode laser power meter. We confirmed that comparable results were obtained with another optical configuration of a back-scattering geometry (figs. S1B to S1E). As a QTF sensor for the FM-AFM operation, we used a qPlus sensor (48) on which a Ag tip was mounted (CreaTec Fischer & Co. GmbH; $Q \approx 10^4$, sample-free resonance frequency $f_0 = 18.8$ kHz; Fig. 1C) and an oscillation controller (Nanonis OC4, SPECS Surface Nano Analysis GmbH). The sine-wave output with a frequency f from the controller was connected to the reference-signal input of a lock-in amplifier (HF2LI, Zurich Instruments), demodulating the PD signals (Fig. 1D).

The quadrature (out-of-phase) component of each harmonics was always zero (see Supplementary Text), while each in-phase components were monitored as an s-SNOM channel.

Tip fabrication

We sharpened and polished the apex of the electrochemically etched Ag tip mounted on the sensor (Fig. 1B) by Ga⁺ FIB milling. During the FIB process, the tunneling-current electrode of the sensor was grounded to prevent charging of the tip. Notably, while the FIB fabrication for STM tips have been reported (15, 59, 69), this is the first report for the FIB process of a tip mounted on a QTF sensor. After the sensor with the FIB-polished tip was introduced into the UHV chamber, the tip apex was further adjusted by mild poking into a clean Ag surface by the STM-based tip-height control to get a strong plasmon resonance (15).

Sample fabrication

we used a single-crystalline Ag(111) surface (MaTeck GmbH) cleaned by multiple cycles of Ar⁺ sputtering and annealing. For the Si/Ag sample preparation (Fig. 4A), we used a home-made Si evaporator placed ~30 cm away from the cleaning stage for the Ag(111) surface in the UHV chamber. The evaporator has a direct-current-heated Si(111) plate (Siegert Wafer GmbH) flash-annealed at 1200 °C. During the Si evaporation, A cleaned Ag(111) sample was heated at 227–230 °C and faced the evaporator.

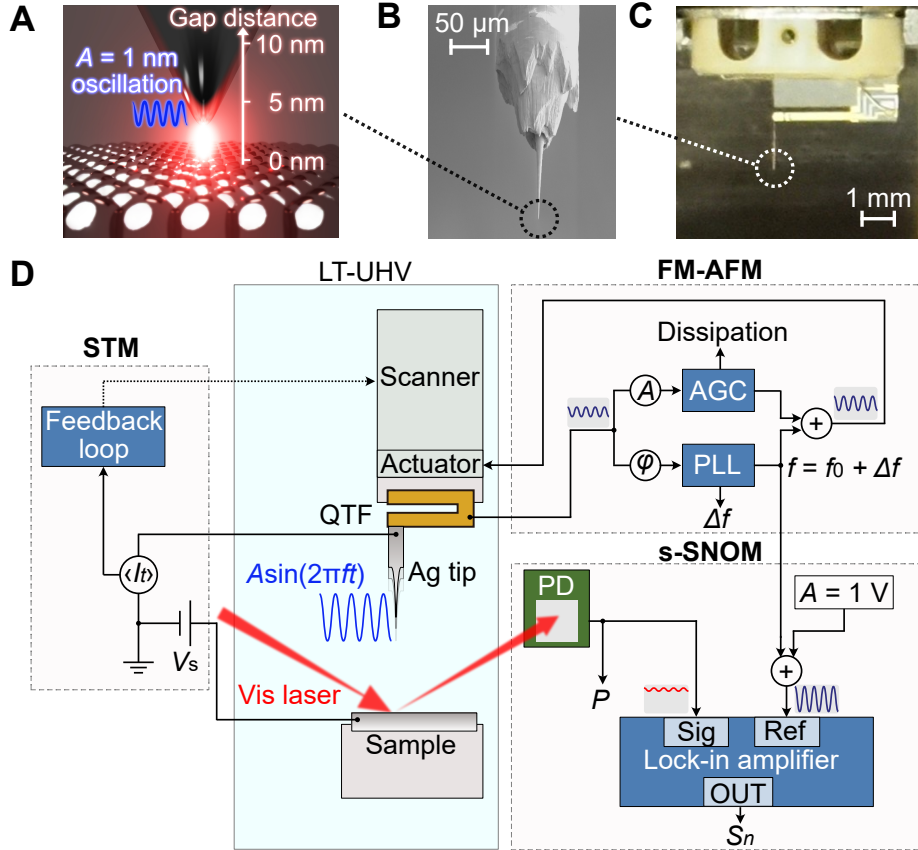


Figure 1: PE-SNOM setup. (A) Schematic of PE-SNOM. Light scattering from the highly confined picocavity-enhanced near-field can be detected by tip oscillation with an amplitude of 1 nm. (B) Scanning electron microscopy image of the apex of an Ag tip after the FIB polishing process. (C) Photo of a QTF sensor with the FIB-polished Ag tip mounted. (D) Circuit diagram of PE-SNOM. The STM/FM-AFM unit is located in an UHV chamber at 8 K. A focused 633-nm laser beam illuminates the junction from outside the chamber and scattering light is collected by a PD outside the chamber. The PD signal is demodulated by a lock-in amplifier using the cantilever oscillation frequency f as a reference.

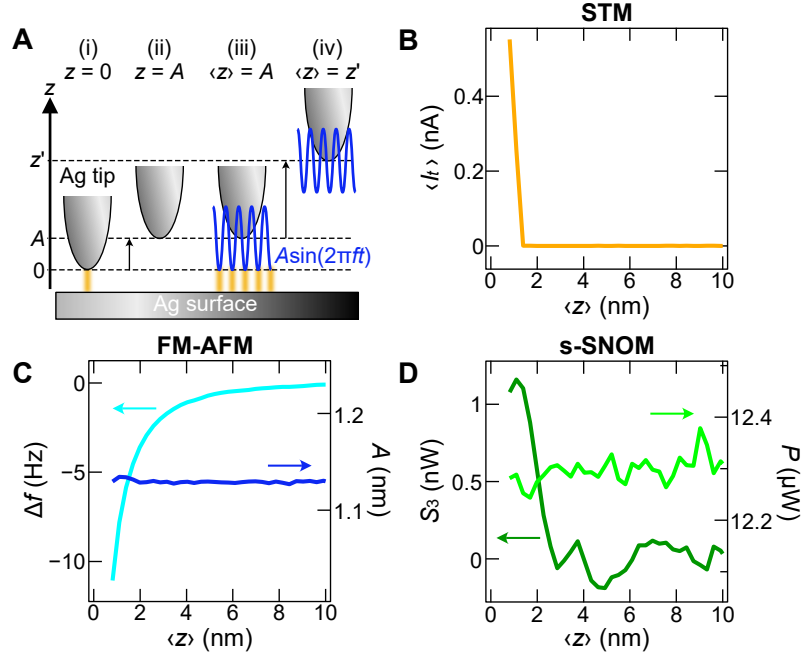


Figure 2: Approach curves of STM, FM-AFM, and s-SNOM. (A) Schematic side-view of the way to obtain an approach curve with an oscillation amplitude A . The origin of z is defined as the tip height determined by the STM set-point (sample bias $V_s = 30$ mV and tunneling current $I_t = 0.10$ nA) without cantilever oscillation, as depicted in (i). After the tip retraction by A (ii), the oscillation is started (iii). At the point, the tip height is described as $z(t) = A[1 + \sin(2\pi ft)]$, where $\langle z(t) \rangle = A$ and $\min[z(t)] = 0$. Then the tip is moved vertically to a given point $\langle z \rangle = z'$ (iv) to record an approach curve. The orange lines between the tip and sample depict tunneling current. (B to D) Approach curves of STM ($\langle I_t \rangle$), FM-AFM (A and Δf), and s-SNOM (P and S_3), respectively, recorded over an Ag(111) terrace ($P_{\text{inc}} = 3$ mW, $A = 1.13$ nm).

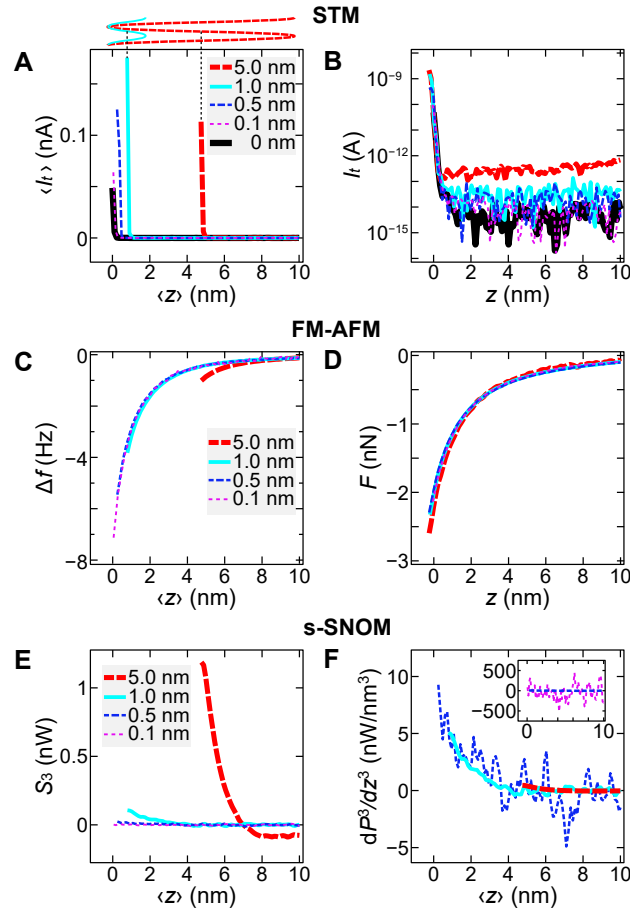


Figure 3: Amplitude-dependent approach curves and their converted/normalized curves. (A) Approach curves of $\langle I_t \rangle$ recorded over an Ag(111) terrace for different oscillation amplitudes A ($P_{\text{inc}} = 6 \text{ mW}$). The sine waves on top of the graph illustrate the tip trajectories during the cantilever oscillation with $A = 5.0 \text{ nm}$ (red dotted curve) and 1.0 nm (cyan solid) at the minimum $\langle z \rangle$ points in the plots. (B) $I_t(z)$ curves converted from (A). (C) Approach curves of Δf simultaneously recorded with (A). (D) $F(z)$ curves converted from (C). (E) Approach curves for S_3 simultaneously recorded with (A). (F) Normalized s-SNOM curves calculated from (E). The normalized curve with the lowest amplitude ($A = 0.1 \text{ nm}$) is not shown in the main graph of (F) but in the inset (magenta dotted curve) because of the large noise. As a reference, the curve with $A = 0.5 \text{ nm}$ (blue dashed curves) is also shown in the inset. With any A , the origin of z is defined as the tip height determined by the STM set-point at $V_s = 30 \text{ mV}$, $I_t = 0.10 \text{ nA}$ without oscillation (see Fig. 2A).

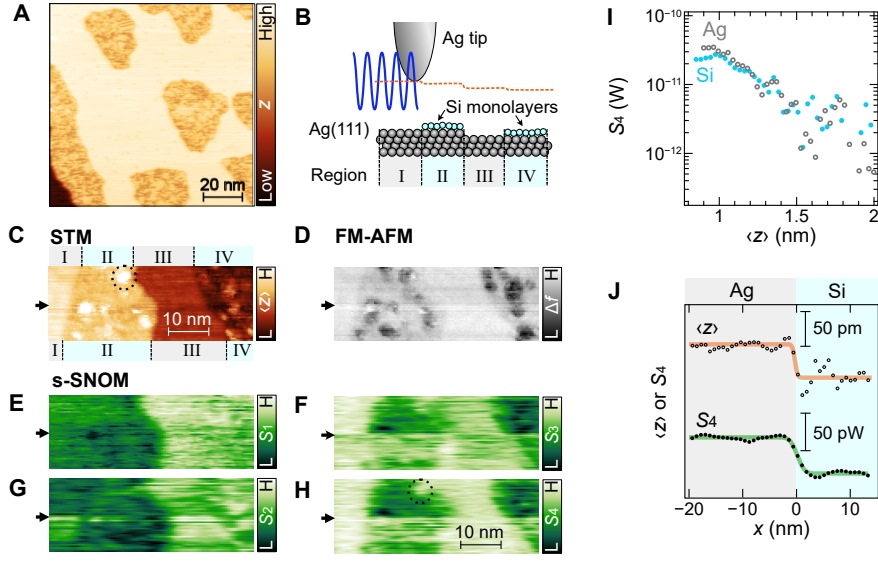


Figure 4: Simultaneously acquired STM, FM-AFM, and s-SNOM images. (A) Typical STM image of amorphous Si monolayer islands on Ag(111) obtained with the FIB-polished Ag tip without laser illumination (set-point: $V_s = 1$ V and $I_t = 0.1$ nA without cantilever oscillation). (B) Side-view scheme of the atomic structures of the sampling area. Regions I–IV correspond to the bare Ag on the upper terrace, Si island on the upper terrace, bare Ag on the lower terrace, and Si island on the lower terrace, respectively. The orange dotted line schematically indicates the tip-height trajectory. (C) STM topography, (D) FM-AFM Δf map, and (E to H) s-SNOM S_1 to S_4 maps simultaneously obtained with laser illumination (STM set-point: $V_s = 30$ mV, $\langle I_t \rangle = 0.10$ nA, $A = 1.0$ nm; $P_{\text{inc}} = 6$ mW). The arrows indicate the position when the tip-apex structure accidentally changed. The black dotted circles in (C) and (H) mark a nanocluster in region II. (I) Approach curves of S_4 recorded over an Ag terrace (gray empty bullets) and an Si island on it (cyan filled bullets). The origin of $\langle z \rangle$ for both plots is defined by the STM set-point over the Ag terrace (set-point: $V_s = 30$ mV and $I_t = 0.10$ nA without oscillation). (J) Line profiles of the STM topographic height $\langle z \rangle$ (upper) and S_4 (bottom) across an Ag–Si boundary on an identical terrace (see fig. S4 indicating the sampling area). The solid curves are the fitting curves with error functions $y = \frac{y_1+y_2}{2} + \frac{y_2-y_1}{2} \text{erf}\left(\frac{x-x_0}{\sqrt{2}\sigma}\right)$, where y_1 (y_2) is the $\langle z \rangle$ or S_4 value before (after) the boundary position x_0 and σ denotes the full width at half maximum.

References and Notes

1. J. F. Schultz, S. Li, S. Jiang, N. Jiang, Optical scanning tunneling microscopy based chemical imaging and spectroscopy. *J. Phys.: Condens. Matter* **32**, 463001 (2020).
2. R. Gutzler, M. Garg, C. R. Ast, K. Kuhnke, K. Kern, Light–matter interaction at atomic scales. *Nat. Rev. Phys.* **3**, 441–453 (2021).
3. M. Müller, Imaging surfaces at the space–time limit: New perspectives of time-resolved scanning tunneling microscopy for ultrafast surface science. *Prog. Surf. Sci.* p. 100727 (2023).
4. H. Lee, *et al.*, Tip-enhanced photoluminescence nano-spectroscopy and nano-imaging. *Nanophotonics* **9**, 3089–3110 (2020).
5. X. Wang, S.-C. Huang, S. Hu, S. Yan, B. Ren, Fundamental understanding and applications of plasmon-enhanced Raman spectroscopy. *Nat. Rev. Phys.* **2**, 253–271 (2020).
6. R. Zhang, *et al.*, Chemical mapping of a single molecule by plasmon-enhanced Raman scattering. *Nature* **498**, 82–86 (2013).
7. J. Lee, K. T. Crampton, N. Tallarida, V. A. Apkarian, Visualizing vibrational normal modes of a single molecule with atomically confined light. *Nature* **568**, 78–82 (2019).
8. X. Qiu, G. Nazin, W. Ho, Vibrationally resolved fluorescence excited with submolecular precision. *Science* **299**, 542–546 (2003).
9. K. Kuhnke, C. Grosse, P. Merino, K. Kern, Atomic-scale imaging and spectroscopy of electroluminescence at molecular interfaces. *Chem. Rev.* **117**, 5174–5222 (2017).
10. B. Yang, *et al.*, Sub-nanometre resolution in single-molecule photoluminescence imaging. *Nature Photon.* **14**, 693–699 (2020).
11. H. Imada, *et al.*, Single-molecule laser nanospectroscopy with micro–electron volt energy resolution. *Science* **373**, 95–98 (2021).
12. E. Kazuma, J. Jung, H. Ueba, M. Trenary, Y. Kim, STM studies of photochemistry and plasmon chemistry on metal surfaces. *Prog. Surf. Sci.* **93**, 163–176 (2018).

13. X. Zhu, Y. Xu, C. Zhao, C. Jia, X. Guo, Recent Advances in Photochemical Reactions on Single-Molecule Electrical Platforms. *Macromol. Rapid Commun.* **43**, 2200017 (2022).
14. A. Ros lawska, *et al.*, Submolecular-scale control of phototautomerization. *Nat. Nanotechnol.* **19**, 738–743 (2024).
15. Y. Park, *et al.*, Atomic-Precision Control of Plasmon-Induced Single-Molecule Switching in a Metal–Semiconductor Nanojunction. *Nat. Commun.* **15**, 6709 (2024).
16. M. Imai-Imada, *et al.*, Orbital-resolved visualization of single-molecule photocurrent channels. *Nature* **603**, 829–834 (2022).
17. F. Benz, *et al.*, Single-molecule optomechanics in “picocavities”. *Science* **354**, 726–729 (2016).
18. M. Barbry, *et al.*, Atomistic near-field nanoplasmonics: reaching atomic-scale resolution in nanooptics. *Nano Lett.* **15**, 3410–3419 (2015).
19. M. Urbieto, *et al.*, Atomic-scale lightning rod effect in plasmonic picocavities: A classical view to a quantum effect. *ACS Nano* **12**, 585–595 (2018).
20. A. Shiotari, T. Kumagai, M. Wolf, Tip-enhanced Raman spectroscopy of graphene nanoribbons on Au(111). *J. Phys. Chem. C* **118**, 11806–11812 (2014).
21. C. Carnegie, *et al.*, Room-temperature optical picocavities below 1 nm³ accessing single-atom geometries. *J. Phys. Chem. Lett.* **9**, 7146–7151 (2018).
22. R. Hillenbrand, B. Knoll, F. Keilmann, Pure optical contrast in scattering-type scanning near-field microscopy. *J. Microsc.* **202**, 77–83 (2001).
23. X. Chen, *et al.*, Modern scattering-type scanning near-field optical microscopy for advanced material research. *Adv. Mater.* **31**, 1804774 (2019).
24. B. Knoll, F. Keilmann, Enhanced dielectric contrast in scattering-type scanning near-field optical microscopy. *Opt. Commun.* **182**, 321–328 (2000).
25. M. B. Raschke, C. Lienau, Apertureless near-field optical microscopy: Tip–sample coupling in elastic light scattering. *Appl. Phys. Lett.* **83**, 5089–5091 (2003).

26. J. Chen, *et al.*, Optical nano-imaging of gate-tunable graphene plasmons. *Nature* **487**, 77–81 (2012).
27. Z. Fei, *et al.*, Gate-tuning of graphene plasmons revealed by infrared nano-imaging. *Nature* **487**, 82–85 (2012).
28. D. Basov, M. Fogler, F. García de Abajo, Polaritons in van der Waals materials. *Science* **354**, aag1992 (2016).
29. T. Low, *et al.*, Polaritons in layered two-dimensional materials. *Nat. Mater.* **16**, 182–194 (2017).
30. M. M. Qazilbash, *et al.*, Mott transition in VO₂ revealed by infrared spectroscopy and nano-imaging. *Science* **318**, 1750–1753 (2007).
31. A. McLeod, *et al.*, Nanotextured phase coexistence in the correlated insulator V₂O₃. *Nat. Phys.* **13**, 80–86 (2017).
32. I. Amenabar, *et al.*, Structural analysis and mapping of individual protein complexes by infrared nanospectroscopy. *Nat. Commun.* **4**, 2890 (2013).
33. J. Nishida, *et al.*, Sub-Tip-Radius Near-Field Interactions in Nano-FTIR Vibrational Spectroscopy on Single Proteins. *Nano Lett.* **24**, 836–843 (2024).
34. R. Jacob, *et al.*, Intersublevel spectroscopy on single InAs-quantum dots by terahertz near-field microscopy. *Nano Lett.* **12**, 4336–4340 (2012).
35. M. Eisele, *et al.*, Ultrafast multi-terahertz nano-spectroscopy with sub-cycle temporal resolution. *Nat. Photon.* **8**, 841–845 (2014).
36. M. Zizlsperger, *et al.*, In situ nanoscopy of single-grain nanomorphology and ultrafast carrier dynamics in metal halide perovskites. *Nat. Photon.* pp. 975–981 (2024).
37. S. Mastel, *et al.*, Understanding the image contrast of material boundaries in IR nanoscopy reaching 5 nm spatial resolution. *ACS Photon.* **5**, 3372–3378 (2018).
38. F. Wang, *et al.*, High resolution and high signal-to-noise ratio imaging with near-field high-order optical signals. *Nano Res.* **15**, 8345–8350 (2022).

39. E. Betzig, R. J. Chichester, Single molecules observed by near-field scanning optical microscopy. *Science* **262**, 1422–1425 (1993).
40. Z. Zafar, *et al.*, Recent development in defects engineered photocatalysts: an overview of the experimental and theoretical strategies. *Energy Environ. Mater.* **5**, 68–114 (2022).
41. F. Zenhausern, Y. Martin, H. Wickramasinghe, Scanning interferometric apertureless microscopy: optical imaging at 10 Angstrom resolution. *Science* **269**, 1083–1085 (1995).
42. J. Koglin, U. C. Fischer, H. Fuchs, Material contrast in scanning near-field optical microscopy at 1–10 nm resolution. *Phys. Rev. B* **55**, 7977 (1997).
43. R. Hillenbrand, F. Keilmann, Material-specific mapping of metal/semiconductor/dielectric nanosystems at 10 nm resolution by backscattering near-field optical microscopy. *Appl. Phys. Lett.* **80**, 25–27 (2002).
44. F. Huth, *et al.*, Nano-FTIR absorption spectroscopy of molecular fingerprints at 20 nm spatial resolution. *Nano Lett.* **12**, 3973–3978 (2012).
45. K.-T. Lin, S. Komiyama, Y. Kajihara, Tip size dependence of passive near-field microscopy. *Opt. Lett.* **41**, 484–487 (2016).
46. F. J. Giessibl, Forces and frequency shifts in atomic-resolution dynamic-force microscopy. *Phys. Rev. B* **56**, 16010 (1997).
47. T. R. Albrecht, P. Grütter, D. Horne, D. Rugar, Frequency modulation detection using high-Q cantilevers for enhanced force microscope sensitivity. *J. Appl. Phys.* **69**, 668–673 (1991).
48. F. J. Giessibl, High-speed force sensor for force microscopy and profilometry utilizing a quartz tuning fork. *Appl. Phys. Lett.* **73**, 3956–3958 (1998).
49. F. J. Giessibl, The qPlus sensor, a powerful core for the atomic force microscope. *Rev. Sci. Instrum.* **90** (2019).
50. T. Siday, *et al.*, All-optical subcycle microscopy on atomic length scales. *Nature* **629**, 329–334 (2024).

51. U. C. Fischer, D. Pohl, Observation of single-particle plasmons by near-field optical microscopy. *Phys. Rev. Lett.* **62**, 458 (1989).
52. F. Huth, *et al.*, Resonant antenna probes for tip-enhanced infrared near-field microscopy. *Nano Lett.* **13**, 1065–1072 (2013).
53. R.-H. Jiang, *et al.*, Near-field plasmonic probe with super resolution and high throughput and signal-to-noise ratio. *Nano Lett.* **18**, 881–885 (2018).
54. J. Döring, H.-G. von Ribbeck, M. Fehrenbacher, S. C. Kehr, L. M. Eng, Near-field resonance shifts of ferroelectric barium titanate domains upon low-temperature phase transition. *Appl. Phys. Lett.* **105** (2014).
55. M. Dapolito, *et al.*, Scattering-type scanning near-field optical microscopy with Akiyama piezo-probes. *Appl. Phys. Lett.* **120** (2022).
56. A. Naber, H.-J. Maas, K. Razavi, U. Fischer, Dynamic force distance control suited to various probes for scanning near-field optical microscopy. *Rev. Sci. Instrum.* **70**, 3955–3961 (1999).
57. P. G. Gucciardi, G. Bachelier, A. Mlayah, M. Allegrini, Interferometric measurement of the tip oscillation amplitude in apertureless near-field optical microscopy. *Rev. Sci. Instrum.* **76** (2005).
58. N. Satoh, K. Kobayashi, K. Matsushige, H. Yamada, Near-field light detection of a photo induced force by atomic force microscopy with frequency modulation. *Jpn. J. Appl. Phys.* **56**, 08LB03 (2017).
59. S. Liu, *et al.*, Resolving the correlation between tip-enhanced resonance Raman scattering and local electronic states with 1 nm resolution. *Nano Lett.* **19**, 5725–5731 (2019).
60. Y.-h. Zhang, P. Wahl, K. Kern, Quantum point contact microscopy. *Nano Lett.* **11**, 3838–3843 (2011).
61. M. Ternes, *et al.*, Interplay of conductance, force, and structural change in metallic point contacts. *Phys. Rev. Lett.* **106**, 016802 (2011).

62. J. E. Sader, Y. Sugimoto, Accurate formula for conversion of tunneling current in dynamic atomic force spectroscopy. *Appl. Phys. Lett.* **97** (2010).
63. J. E. Sader, S. P. Jarvis, Accurate formulas for interaction force and energy in frequency modulation force spectroscopy. *Appl. Phys. Lett.* **84**, 1801–1803 (2004).
64. D. Solonenko, O. D. Gordan, G. Le Lay, D. R. Zahn, P. Vogt, Comprehensive Raman study of epitaxial silicene-related phases on Ag(111). *Beilstein J. Nanotechnol.* **8**, 1357–1365 (2017).
65. J. F. Schultz, N. Jiang, Characterizations of two-dimensional materials with cryogenic ultrahigh vacuum near-field optical microscopy in the visible range. *J. Vac. Sci. Technol. A* **40**, 040801 (2022).
66. Z. Majzik, *et al.*, Combined AFM and STM measurements of a silicene sheet grown on the Ag(111) surface. *J. Phys.: Condens. Matter* **25**, 225301 (2013).
67. N. Ocelic, A. Huber, R. Hillenbrand, Pseudoheterodyne detection for background-free near-field spectroscopy. *Appl. Phys. Lett.* **89** (2006).
68. B. Hecht, H. Bielefeldt, Y. Inouye, D. Pohl, L. Novotny, Facts and artifacts in near-field optical microscopy. *J. Appl. Phys.* **81**, 2492–2498 (1997).
69. H. Böckmann, *et al.*, Near-field spectral response of optically excited scanning tunneling microscope junctions probed by single-molecule action spectroscopy. *J. Phys. Chem. Lett.* **10**, 2068–2074 (2019).

Acknowledgments

Funding: F.S. acknowledges financial support from grant PID2022-140845OBC61 and the Ramón y Cajal fellowship RYC2021-034304-I. T.K. acknowledges the support of JST FOREST Grant No. JPMJFR201J.

Author contributions: A.S., M.W., T.K., and M.M. directed the project. A.S., J.N., and T.K. designed and constructed the experimental setup. A.H. conducted the FIB-polishing process of the

Ag tip mounted on the QTF sensor. A.S. performed the experiments and analyzed the data. A.S., F.S., M.W., and M.M. discussed the data interpretation. A.S. wrote the manuscript and all authors participated in revisions of the manuscript.

Competing interests: There are no competing interests to declare.

Data and materials availability: All data needed to evaluate the conclusions in the paper are present in the paper and/or the Supplementary Materials.

Supplementary materials

Supplementary Text

Figs. S1 to S4

Supplementary Materials for
Picocavity-enhanced near-field optical microscopy with 1 nm
resolution

Akitoshi Shiotari*, Jun Nishida, Adnan Hammud, Fabian Schulz, Martin Wolf, Takashi Kumagai,
Melanie Müller

*Corresponding author. Email: shiotari@fhi-berlin.mpg.de

This PDF file includes:

Supplementary Text

Figures S1 to S4

Supplementary Text

Here, we show the detail of the Taylor series for the scattered light intensity P modulated by the cantilever oscillation with an amplitude of A and a frequency of f (Eq. 1 in the main text);

$$\begin{aligned}
 P[z(t)] &= P[\langle z \rangle + A \sin \theta] \\
 &= P(\langle z \rangle) \\
 &\quad + AP^{(1)}(\langle z \rangle) \sin \theta \\
 &\quad + \frac{1}{2}A^2P^{(2)}(\langle z \rangle) \sin^2 \theta \\
 &\quad + \frac{1}{6}A^3P^{(3)}(\langle z \rangle) \sin^3 \theta \\
 &\quad + \frac{1}{24}A^4P^{(4)}(\langle z \rangle) \sin^4 \theta \\
 &\quad + \frac{1}{120}A^5P^{(5)}(\langle z \rangle) \sin^5 \theta \\
 &\quad + \frac{1}{720}A^6P^{(6)}(\langle z \rangle) \sin^6 \theta + \dots, \tag{S1}
 \end{aligned}$$

where $\theta \equiv 2\pi ft$. Using multiple-angle formulas, $\sin^m \theta$ can be expanded as follows;

$$\begin{aligned}
 P[z(t)] &= P(\langle z \rangle) \\
 &\quad + AP^{(1)}(\langle z \rangle) \sin \theta \\
 &\quad + \frac{1}{4}A^2P^{(2)}(\langle z \rangle) (1 - \cos 2\theta) \\
 &\quad + \frac{1}{24}A^3P^{(3)}(\langle z \rangle) (3 \sin \theta - \sin 3\theta) \\
 &\quad + \frac{1}{192}A^4P^{(4)}(\langle z \rangle) (3 - 4 \cos 2\theta + \cos 4\theta) \\
 &\quad + \frac{1}{1920}A^5P^{(5)}(\langle z \rangle) (10 \sin \theta - 5 \sin 3\theta + \sin 5\theta) \\
 &\quad + \frac{1}{23040}A^6P^{(6)}(\langle z \rangle) (10 - 15 \cos 2\theta + 6 \cos 4\theta - \cos 6\theta) + \dots. \tag{S2}
 \end{aligned}$$

As described in Eq. 2 of the main text, the lock-in signal corresponds to

$$S_n(\langle z \rangle) = \langle P[z(t)] \sin(n\theta + \phi_n) \rangle \tag{S3}$$

for the n -th harmonics. Among the components of $\sin(m\theta)$ or $\cos(m\theta)$ in Eq. S2, only the component at $m = n$ gives a non-zero time-averaged value, as $\langle \sin^2 n\theta \rangle = \langle \cos^2 n\theta \rangle = \frac{1}{2}$. For example, the first

harmonic signal S_1 is maximized at $\phi_1 = 0$ as

$$\begin{aligned}
S_1(\langle z \rangle) &= \langle P[z(t)] \sin \theta \rangle \\
&= AP^{(1)}(\langle z \rangle) \langle \sin^2 \theta \rangle \\
&\quad + \frac{1}{24} A^3 P^{(3)}(\langle z \rangle) \langle 3 \sin^2 \theta \rangle \\
&\quad + \frac{1}{1920} A^5 P^{(5)}(\langle z \rangle) \langle 10 \sin^2 \theta \rangle + \dots \\
&= \frac{1}{2} AP^{(1)}(\langle z \rangle) + \frac{3}{48} A^3 P^{(3)}(\langle z \rangle) + \frac{1}{384} A^5 P^{(5)}(\langle z \rangle) + \dots .
\end{aligned} \tag{S4}$$

In a similar manner, each lock-in signal is maximized at $\phi_n = -\frac{n-1}{2}\pi$ as

$$S_2(\langle z \rangle) = \frac{1}{8} A^2 P^{(2)}(\langle z \rangle) + \frac{1}{96} A^4 P^{(4)}(\langle z \rangle) + \frac{1}{3072} A^6 P^{(6)}(\langle z \rangle) + \dots , \tag{S5}$$

$$S_3(\langle z \rangle) = \frac{1}{48} A^3 P^{(3)}(\langle z \rangle) + \frac{1}{768} A^5 P^{(5)}(\langle z \rangle) + \dots , \tag{S6}$$

$$S_4(\langle z \rangle) = \frac{1}{384} A^4 P^{(4)}(\langle z \rangle) + \frac{1}{7680} A^6 P^{(6)}(\langle z \rangle) + \dots . \tag{S7}$$

Equation 3 in the main text corresponds to a simplified description of Equations S4 to S7. Note that practically, depending on the lock-in amplifier, the experimental phase values ϕ_n can shift from the theoretical values. Assuming that $P^{(5)}$, $P^{(6)}$, and higher order derivatives are negligibly small, the n -th derivative of the scattering laser power P with respect to $\langle z \rangle$ is described using the lock-in signals S_n as follows:

$$P^{(1)}(\langle z \rangle) \approx \frac{2}{A} [S_1(\langle z \rangle) - 3S_3(\langle z \rangle)] , \tag{S8}$$

$$P^{(2)}(\langle z \rangle) \approx \frac{8}{A^2} [S_2(\langle z \rangle) - 4S_4(\langle z \rangle)] , \tag{S9}$$

$$P^{(3)}(\langle z \rangle) \approx \frac{48}{A^3} S_3(\langle z \rangle) , \tag{S10}$$

$$P^{(4)}(\langle z \rangle) \approx \frac{384}{A^4} S_4(\langle z \rangle) . \tag{S11}$$

Figures S3A, D, G, and J show the approach curves of S_1 to S_4 , respectively, recorded with several oscillation amplitudes $A = 0.1$ – 5.0 nm. Using different A provides different curve appearances, but the curves can be matched by the normalization. Figures S3B, E, H, and K show the $P^{(1)}(\langle z \rangle)$ to $P^{(4)}(\langle z \rangle)$ curves calculated from Eqs. S8 to S11, respectively. Each n -th derivative value is consistent with any A used. On the one hand, small A causes severe noise at higher n due to the coefficient of $1/A^n$ in the equations. For example, in the third (fourth) derivative channel, the

normalized curve(s) with $A = 0.1$ nm ($A = 0.5$ and 0.1 nm) is (are) too noisy to read the signal appearance like an exponential function [Figs. S3H and J (K and L)]. On the other hand, with a too large A , higher order harmonics components is no longer negligible in S_n signals. For example, as shown in Eq. S4, the S_1 curve has the contribution of $A^3P^{(3)}(\langle z \rangle)$ in addition to the major factor of $AP^{(1)}(\langle z \rangle)$. As a result, the raw approach curves with $A = 5.0$ nm (Figs. S3A and D) appear to deviate significantly from the curves with the other smaller A . Figure S3C (S3F) show the first (second) derivative curve reproduced by only considering S_1 (S_2) signals, i.e., assuming that $d^n P/dz^n \approx 2^n n! A^{-n} S_n$. In this rough approximation, the calculated curve with $A = 5.0$ nm does not match those with the other A (Figs. S3C and F). In contrast, as described above, the more accurate approximation using Eqs. S8 and S9 improves the matching (Figs. S3B and E). Note that the calculated dP/dz curve with $A = 5.0$ nm still deviates slightly from the other curves, possibly due to the contribution of higher harmonics, i.e., $A^5P^{(5)}$ in Eq. S4. Therefore, from the dataset, $A = 1.0$ nm is the optimal condition under which all the S_1 to S_4 channels well reproduce the n -th differential curves with a reasonable signal-to-noise ratio. Note that as mentioned in the main text, the optimal amplitude value is expected to depend on the experimental setup used, such as the tip apex structure and the efficiency of the light collection.

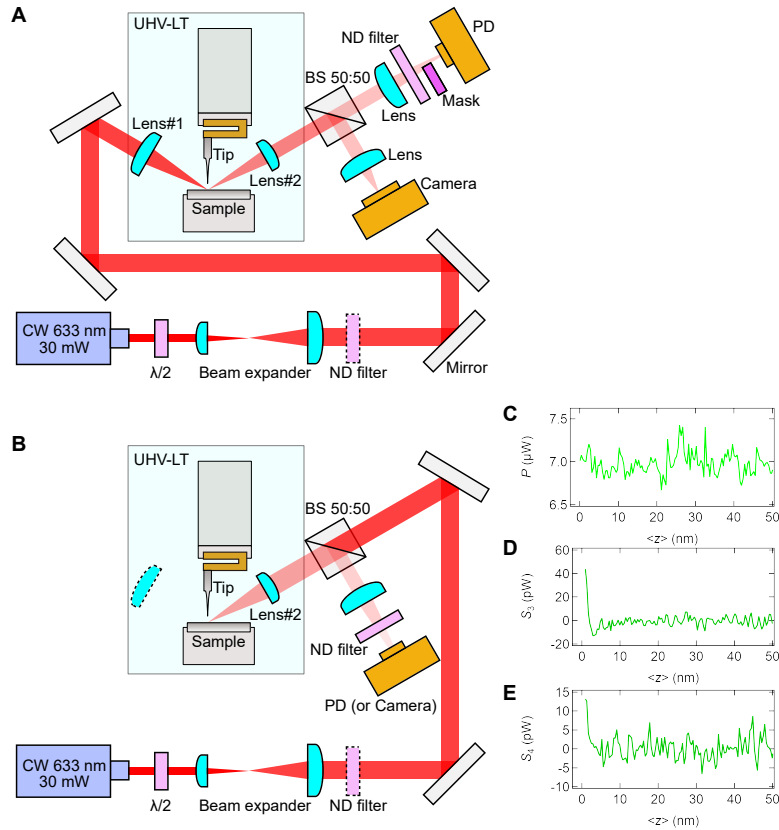


Figure S1: Two optical configurations for PE-SNOM. (A) Configuration we mainly used. Continuous-wave 633-nm laser output entered into the UHV chamber and was focused into the tip–sample junction via Lens #1 (NA = 0.4) mounted in the STM/FM-AFM unit. The scattering light from the junction was collected by Lens #2 (NA = 0.2) together with reflecting light and was directed outside the chamber to a PD through an neutral density (ND) filter and a mask. To adjust the scattering light intensity to a PD-detectable range, the mask was used for blocking the strong light directly reflecting by the sample independent of the tip existence. (B) Another optical configuration of a back-scattering geometry. Lens #2 was used both for incident light focusing and for scattering light collection. The scattering light was directed to the PD via a beam splitter (BS). (C to E) Approach curves of P , S_3 , and S_4 , respectively, recorded over a bare Ag(111) terrace with the configuration in (B). The high harmonics s-SNOM channels have signals in a very close tip–sample gap, which is in good agreement with the results with the configuration in (A). This verifies that both configurations are capable of PE-SNOM measurements. Nevertheless, the s-SNOM signals in the latter configuration (B) are generally weaker than those in the former (A) because in the latter configuration, the incident laser intensity is reduced by passing through the BS.

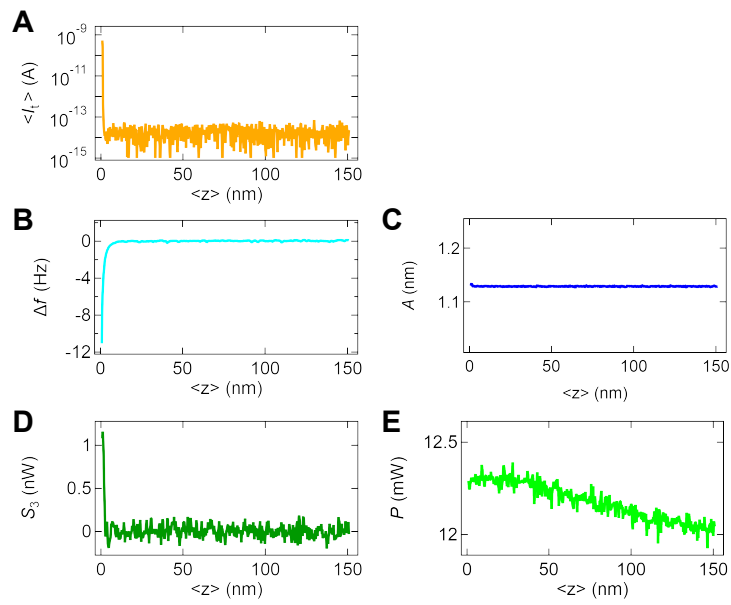


Figure S2: The same approach curves as those shown in Figs. 2B to 2D of the main text, but with the full tip-height range recorded. (A) $\langle I_t \rangle$, (B) Δf , (C) A , (D) S_3 , and (E) P .

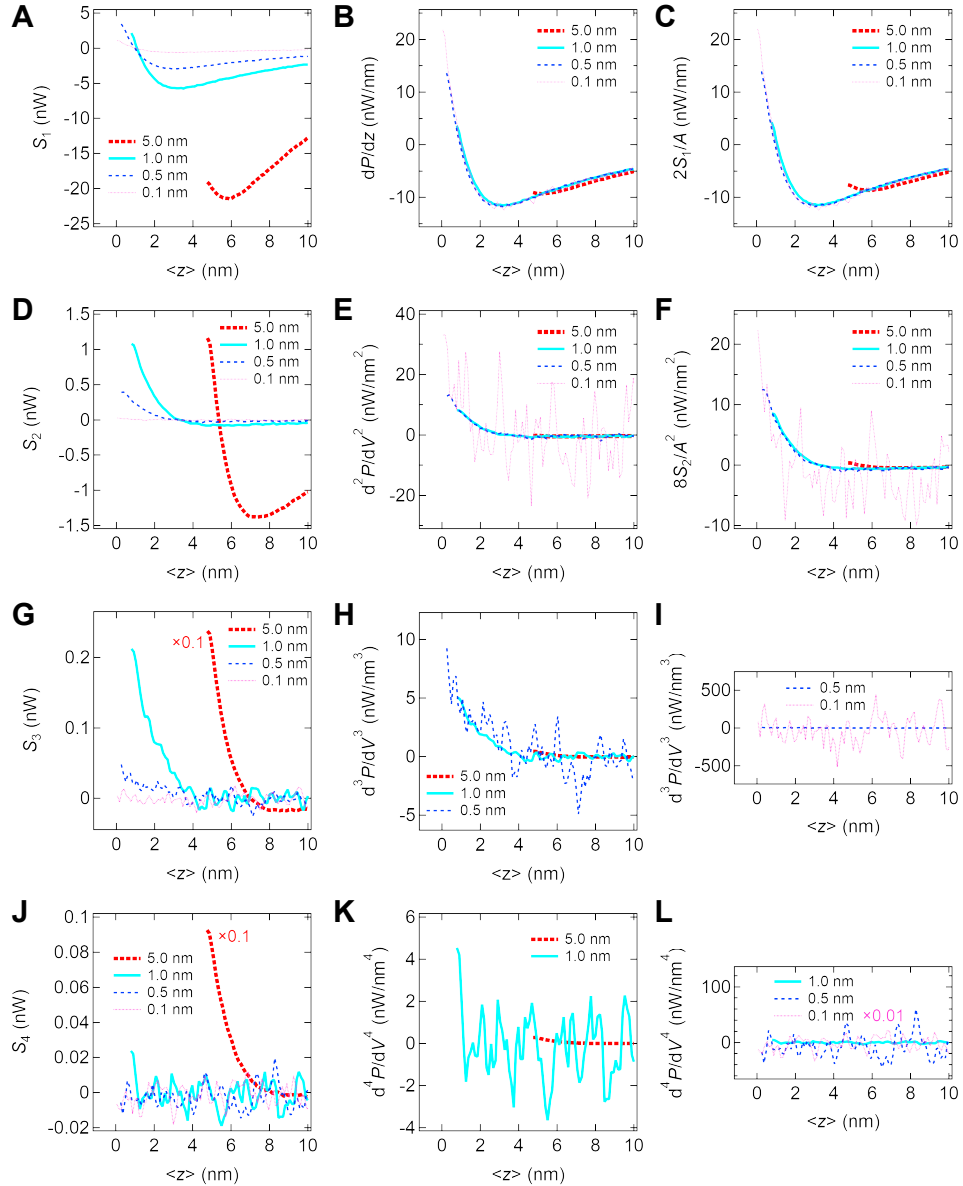


Figure S3: Approach curves of S_n with different A and their normalized curves. (A) S_1 , (B) $P^{(1)}$ calculated from S_1 and S_3 , and (C) $P^{(1)}$ calculated only from S_1 . (D) S_2 , (E) $P^{(2)}$ calculated from S_2 and S_4 , and (F) $P^{(2)}$ calculated only from S_2 . (G) S_3 , (H) $P^{(3)}$ calculated from S_3 with larger A , and (I) $P^{(3)}$ calculated from S_3 with lower A . (J) S_4 , (K) $P^{(4)}$ calculated from S_4 with larger A , and (L) $P^{(4)}$ calculated from S_4 with lower A . The plots in (G) to (I) are the same as those shown in Figs. 3E and 3F of the main text.

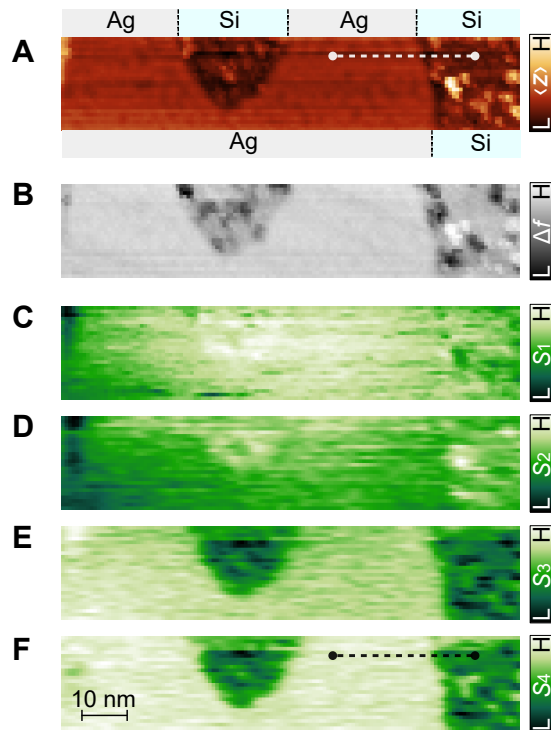


Figure S4: Simultaneously acquired STM, FM-AFM, and s-SNOM images of a different area from that for Figs. 4C to 4H in the main text. (A) STM topography ($\langle z \rangle$), (B) FM-AFM channel (Δf), and (C to F) s-SNOM channel (S_1 to S_4). Dotted line in (A) and (F) correspond to the position where the line profiles in Fig. 4J of the main text were taken. The area was selected for the line profiles because the flat Ag terrace and Si island without characteristic defects (such as nanoprotusions) are wider than those in Figs. 4C to 4H of the main text and exists.